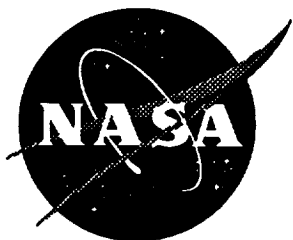NASA Contractor Report 198310

The Sensitivity of Large-Eddy Simulation to Local and Nonlocal Drag Coefficients at the Lower Boundary

D. G. Schowalter, D. S. DeCroix, Y-L. Lin, S. P. Arya, and M. L. Kaplan
North Carolina State University, Raleigh, North Carolina

National Aeronautics and
Space Administration
Langley Research Center
Hampton, Virginia 23681-0001

Abstract

It was found that the homogeneity of the surface drag coefficient plays an important role in the large scale structure of turbulence in large-eddy simulation of the convective atmospheric boundary layer. Particularly when a ground surface temperature was specified, large horizontal anisotropies occurred when the drag coefficient depended upon local velocities and heat fluxes. This was due to the formation of streamwise roll structures in the boundary layer. In reality, these structures have been found to form when shear is approximately balanced by buoyancy. The present cases, however, were highly convective. The formation was caused by particularly low values of the drag coefficient at the entrance to thermal plume structures.

Contents

List of Tables

List of Figures

1 Introduction

The work presented in this paper is part of a joint NASA FAA program to predict aircraft wake vortex behavior under various meteorological conditions within the planetary boundary layer. As described by Hinton (1995), the long term goal is to have safer, more efficient spacing requirements for landing aircraft. In the short term, we plan to simulate wake vortex interaction with atmospheric turbulence. As a first step, we have achieved validated large-eddy simulation of atmospheric boundary layer turbulence in convective conditions and have found some important results with regard to the implementation of the surface stress boundary condition. Some of the validation results are contained in Schowalter et al. (1995).

A number of recent publications have addressed the effects of nonhomogeneous surface heating in large-eddy simulation. Hechtel et al. (1990) have studied the effects of random variations in surface heat flux on large-eddy simulations of the convective boundary layer. They found no significant differences between the homogeneous and nonhomogeneous cases. Shen and Leclerc (1994), however, found that sinusoidal variations in surface heat flux had a significant effect on the turbulence statistics when the mean wind was weak. Shen and Leclerc (1995) further found that the most significant differences in variance structure occurred when the length scales of the sinusoidal variations were on the order of the boundary layer depth.

Large-eddy simulation involves explicit rendering of the large-scale turbulent eddies and a parameterization of the small scale eddies. Thus, the equations are filtered such that small scale motions cannot be resolved. Be-

cause the scales of motion close to the ground are particularly unresolved, calculating the stress there is especially problematic. Past researchers (Deardorff, 1973, 1974, Moeng, 1984, Mason, 1989, Schmidt and Schumann, 1989, among others) have used Monin-Obukhov similarity laws to calculate the stress at the surface. Usually, the local stress at the surface is related to the local velocity near the surface by

$$\tau_0 = -C_D ||\mathbf{u}|| \mathbf{u}, \tag{1}$$

where τ_0 represents the local surface stress, C_D the drag coefficient, u the local horizontal velocity vector, and $||\mathbf{u}||$ is the magnitude of that velocity. The drag coefficient is dependent upon the stability characteristics of the surface and is calculated using the similarity laws. Although the stress is proportional to the square of the *local* velocity, the drag coefficient may or may not be horizontally homogeneous.

Deardorff's (1973, 1974), Mason's (1989), and Schmidt and Schumann's (1989) drag coefficients depended upon local variables, but Moeng's (1984) was based upon horizontal averages of the variables. There is little explanation in any of these cases as to why the choice was made. Deardorff (1973) did explain, however, that Monin-Obukhov similarity laws were based upon long time or ensemble averages and that using them locally was not strictly correct.

In this paper, we compare both approaches and find significant differences in turbulent structure. The LES model and boundary conditions are described in section 2 while sensitivity tests of various domain sizes and resolutions and a discussion of those results are found in section 3. Concluding

2

remarks are made in section 4.

2   Model Description

We have used the TASS model (Proctor 1988; Proctor and Bowles 1992) for the simulations. The model was originally developed for the study of thunderstorms and microbursts, but only required a change in boundary conditions for the simulation of the planetary boundary layer. Not allowing precipitation in the present simulations, the equations solved were

$$
\begin{aligned}
\frac{\partial u_i}{\partial t} = & -\frac{H}{\rho_0}\frac{\partial p}{\partial x_i} + u_i\frac{\partial u_j}{\partial x_j} - \frac{\partial(u_i u_j)}{\partial x_j} \\
& +g(H-1)\delta_{i3} - 2\Omega_j(u_k - u_{g_k})\epsilon_{ijk} \\
& +\frac{1}{\rho_0}\frac{\partial \tau_{ij}}{\partial x_j}
\end{aligned}
\tag{2}
$$

$$
\frac{\partial p}{\partial t} = -\frac{C_p P}{C_v}\frac{\partial u_j}{\partial x_j} + \rho_0 g u_j \delta_{j3}
\tag{3}
$$

$$
\begin{aligned}
\frac{\partial \theta}{\partial t} = & -\frac{1}{\rho_0}\frac{\partial(\theta\rho_0 u_j)}{\partial x_j} + \frac{\theta}{\rho_0}\frac{\partial(\rho_0 u_j)}{\partial x_j} \\
& +\frac{1}{\rho_0}\frac{\partial S_j(\theta)}{\partial x_j}
\end{aligned}
\tag{4}
$$

$$
\begin{aligned}
\frac{\partial Q_v}{\partial t} = & -\frac{1}{\rho_0}\frac{\partial(Q_v \rho_0 u_j)}{\partial x_j} + \\
& \frac{Q_v}{\rho_0}\frac{\partial(\rho_0 u_j)}{\partial x_j} + \frac{1}{\rho_0}\frac{\partial S_j(Q_v)}{\partial x_j}.
\end{aligned}
\tag{5}
$$

Here, u_i are the velocity components, p the pressure deviation from the environment P_0, Ω_j the earth's rotation vector, g the gravitational acceleration,

3

C_p the specific heat at constant pressure, C_v the specific heat at constant volume, ρ_0 the density of the environment, u_{g_k} the geostrophic wind vector, τ_{ij} the subgrid turbulent stress tensor, θ the potential temperature, Q_v the water vapor mixing ratio, and $S_j(Q)$ is the subgrid turbulent flux of the scalar Q. Additionally,

$$H = (\frac{\theta}{\theta_0} - \frac{pC_v}{P_0C_p})[1 + 0.61(Q_v - Q_{v0})], \tag{6}$$

where Q_{v0} is the water vapor mixing ratio of the environment.

A modified Smagorinsky first order closure was used in which the eddy viscosity depended upon stability:

$$\tau_{ij} = \rho_0 K_M D_{ij} = \rho_0 K_M(\frac{\partial u_i}{\partial x_j} +$$
$$\frac{\partial u_j}{\partial x_i} - \frac{2}{3}\frac{\partial u_k}{\partial x_k}\delta_{ij}) \tag{7}$$

$$S_j(\theta) = \rho_0 K_H \frac{\partial \theta}{\partial x_j} \tag{8}$$

$$K_M = (l)^2\sqrt{\frac{1}{2}D_{ij} \cdot D_{ij}(1 - R_f)} \tag{9}$$

where

$$l = \alpha\Delta \qquad kz \geq \alpha\Delta \tag{10}$$

$$l = \frac{\alpha\Delta[1+(\alpha\Delta/kz)^{n-1}]}{1+(\alpha\Delta/kz)^n} \qquad \alpha\Delta > kz > k\Delta z/2 \tag{11}$$

$$l = kz \qquad z \leq \Delta z/2 \tag{12}$$

$$\Delta = (2\Delta x 2\Delta y 2\Delta z)^{1/3} \tag{13}$$

and

$$K_H = 3K_M. \tag{14}$$

4

Here, R_f denotes the local flux Richardson's number, α is an empirical constant, and k is von Karman's constant. The purpose of Equation 11 is to match the mixing length to the appropriate value close to the ground where the flow is under-resolved. For the current runs, the matching parameter, n was set to 2.5.

These equations were solved on an Arakawa C type mesh. Periodic boundary conditions have been used in the horizontal directions, while a sponge layer with three grid intervals has been added on the top of the physical domain. At the top boundary, there existed neither heat nor mass transfer.

The lower boundary employed a no-slip condition. We have used two methods of heat transfer from the ground to the atmosphere. In the first case, the air temperature at a specified level close to the ground has been given as a function of time. The heat flux was then calculated based upon the difference between the atmospheric temperature at the first grid level and the temperature close to the ground. This is useful for comparison to experimental observations in which heat flux was not directly measured, but careful temperature measurements were made. Appendix A gives the details of this calculation. The second method was the explicit specification of surface heat flux as a function of time.

Because the first grid point above the ground is assumed to be within the constant stress surface layer, the drag coefficient could be calculated through the use of Monin-Obukhov similarity laws. The result is

$$C_D = \{\frac{k}{\ln(z_a/z_0) - \Psi_M(z_a/L)}\}^2,\qquad(15)$$

where z_a is the height of the first grid level, z_0 is the roughness height, Ψ_M

is the stability function given by Paulson (1970), and L is the Obukhov length. Specifics of the calculation of Ψ_M may be found in the Appendix. The local velocity at height z_a was then used in Equation (1) to calculate the local stress at the ground. For a horizontally varying drag coefficient, the Obukhov length may be calculated as

$$L = -\frac{\theta u_*^3}{g(\overline{w'\theta'})_s},$$ (16)

where

$$u_* = \frac{ku_a}{\ln(z_a/z_0) - \Psi_M(z_a/L)}.$$ (17)

Here, u_a is the local velocity magnitude at z_a and $(\overline{w'\theta'})_s$ is the local surface heat flux. For a global drag coefficient, we would have

$$L = -\frac{\langle\theta\rangle u_*^3}{g\langle(\overline{w'\theta'})_s\rangle},$$ (18)

and

$$u_* = \frac{k\langle u_a\rangle}{\ln(z_a/z_0) - \Psi_M(z_a/L)},$$ (19)

where $\langle\ \rangle$ denotes a horizontal average over the entire domain. Note that a value of L is required in Equations (17) and (19). The value from the previous time step was used here.

For the homogeneous drag coefficient case, the model has been compared with observations of the Wangara Experiment, Day 33 [4]. Figure 1 (a) shows potential temperatures as a function of local time of day for simulation and observations. The simulation was started from the 0900 local sounding. Figure 1 (b) shows a comparison of mean wind profiles after three hours of simulation. In the latter case, results from Deardorff (1974) are also shown.

Notice that a 40 × 40 × 40 grid was used for this case with 125 m horizontal resolution and 50 m vertical resolution. The model reasonably reproduced the experimental results.

For testing of the boundary conditions, simplified initial and environmental conditions were contrived. All cases to be discussed in section 3 used a constant westerly geostrophic wind of 3.0 ms^{-1}. Winds were initialized at this geostrophic value. The sounding from 1200 local time on Day 33 of the Wangara experiment was used for the initial temperature profile. The inversion was located at approximately 1000 m. Random temperature perturbations with a maximum of $\pm$ 1 C were introduced within the lowest three layers of the grid at initialization to start convection. A total of seven different runs, listed in Table 1, were made with different specifications of surface temperature or heat flux, horizontal domain size, and vertical resolution.

3   Results and Discussion

3.1   70 × 70 × 36 Domain

Cases ALT, ALF, and AGF, discussed here, contained 70 points in both the x (easterly) and y (northerly) directions, while 36 points were used in the z (vertical) direction. Each grid cell had a resolution of 50 m in all directions. This resulted in a domain size of 3500 m × 3500 m × 1800 m with the center of the first grid cell at 25 m above the ground. For case ALT (Local Temperature), the temperature at z=2 m was specified and increased in time at a rate of 0.72 C hr^{-1}. The surface heat flux thus depended upon the local
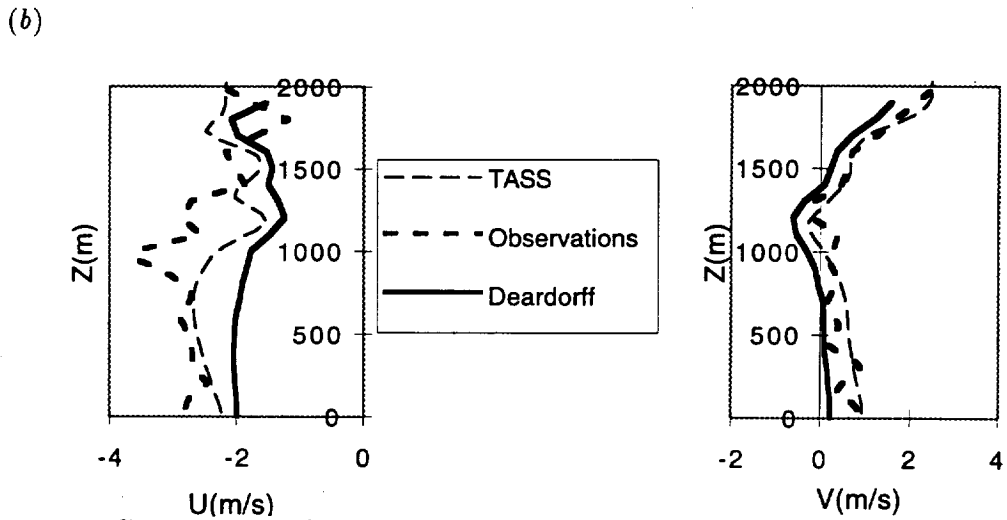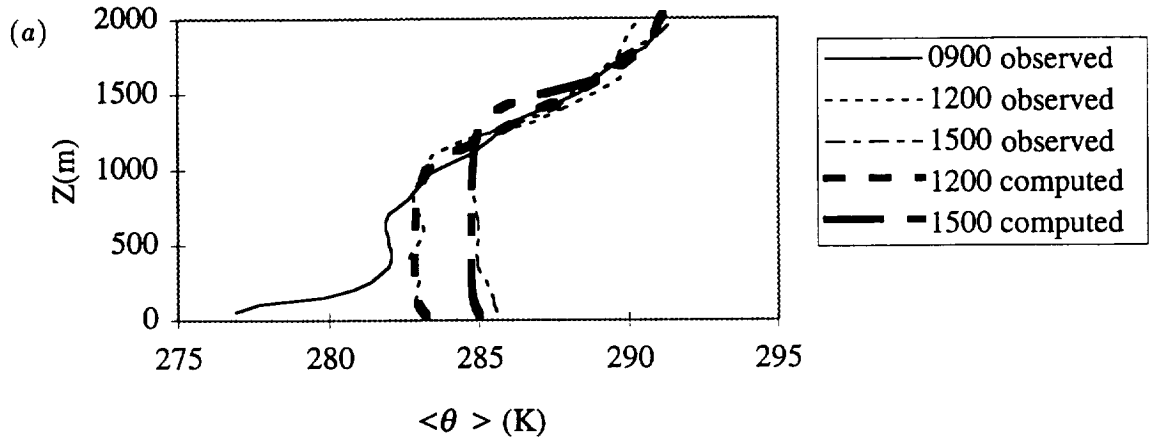
Figure 1: Comparison of model results with the Wangara Experiment, Day 33. (a) Potential temperature profiles at various local times of day. (b) Mean winds at 1200 local time, after three hours of simulation. Also shown are Deardorff's (1974) results.

Abbreviation	Run Description
ALT	Local Drag Coefficient, Surface Temperature Specified
ALF	Local Drag Coefficient, Surface Heat Flux Specified
AGF	Global Drag Coefficient, Surface Heat Flux Specified
BLT	ALT with increased horizontal domain size
BGF	AGF with increased horizontal domain size
CLT	ALT with increased vertical resolution and moderate horizontal domain size
CGF	AGF with increased vertical resolution and moderate horizontal domain size

Table 1: Abbreviations for experiments performed in this study.

temperature difference between $z=2$ m and $z=25$ m. The drag coefficient was then a function of horizontal position. Appendix A contains further details of this calculation. For case ALF (Local Flux), the horizontally averaged surface heat flux was extracted from the ALT run as a function of time and was specified uniformly at the surface. The drag coefficient, however, remained a function of horizontal position. For case AGF (Global Flux), the same value of surface heat flux was used, but the drag coefficient was horizontally homogeneous.

3.1.1 Variances

Figure 2 shows the velocity variance structure throughout the boundary layer for each case mentioned above. These variances were calculated by averaging horizontally over the entire domain every two minutes from 120 minutes to 180 minutes in simulation time. Then, these values were averaged in turn so that the result was an average over time and space. The resolved values of the correlations were added to an estimate of the subgrid contribution. This estimate was calculated by the method of Mason and Thomson (1992). In Figure 2(a), it is noticeable that the horizontal velocity variance was significantly less when the heat flux was uniformly specified and the drag coefficient was nonhomogeneous (ALF). The vertical velocity variance, shown in Figure 2(b), was nearly the same for each case. Figure 2(c) reveals the most striking difference which is in the ratio between the two horizontal velocity variances. For case ALT, in which the surface temperature was specified and the drag coefficient was nonhomogeneous, there are large anisotropies at

10
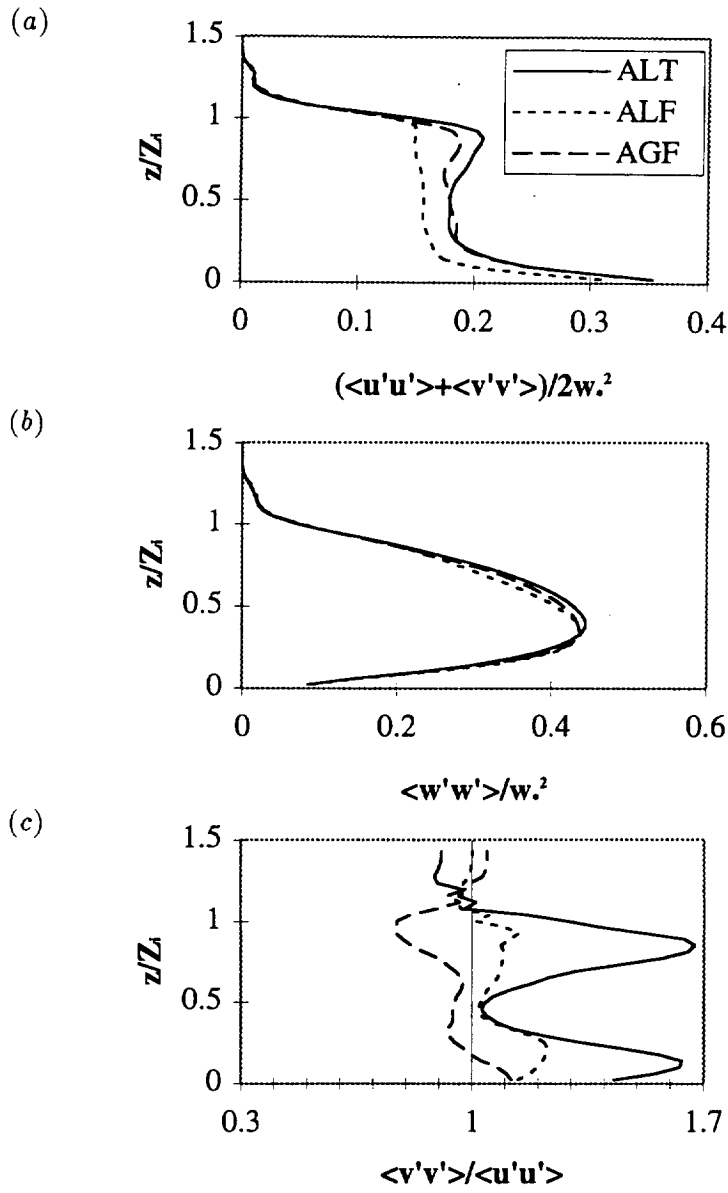
Figure 2: Comparison of cases ALT, ALF, and AGF. (a) horizontal velocity variance, (b) vertical velocity variance, and (c) horizontal anisotropy.

11
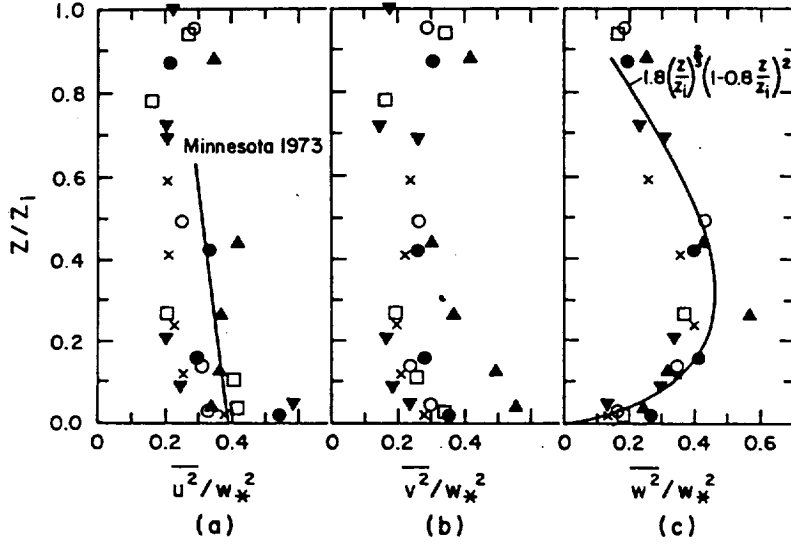
Figure 3: Velocity variances from the AMTEX experiment. Reproduced from Lenschow *et al.* (1980).

the bottom and at the top of the mixed layer. For case ALF, in which the drag coefficient was nonhomogeneous, but the surface heat flux was homogeneously specified, the anisotropy is qualitatively similar to case ALT, but the magnitudes are not as large. For case AGF, in which the drag coefficient was global and the surface heat flux was specified, the horizontal variances are generally equal except near the top of the mixed layer, where $\langle u'u' \rangle$ is larger than $\langle v'v' \rangle$. This latter case seems more reasonable, since the two components are expected to be the same in the mixed layer in convective conditions. It is also expected that $\langle u'u' \rangle$ would be somewhat larger in the entrainment region, since the shear production term is large there, the geostrophic wind being entirely westerly.

Simulated variances may be compared with those measured in the atmo-

12

Symbol	Date	Z_i/L
□	2/15	-17.9
▼	2/16	-40.2
●	2/18	-26.2
×	2/22	-32.4
○	2/24	-61.8
▲	2/26	-13.2

Table 2: Symbols for figure 3.

spheric boundary layer under convective conditions (Lenschow *et al.* 1980)
This data was taken by aircraft during the AMTEX experiment. Table 2
shows the dates and dimensionless inversion heights for the cases shown in
the figure. We see that the simulated variances from Figure 2 are similar to
those in Figure 3, especially for cases ALT and AGF. In terms of anisotropy,
we see that $\langle v'v' \rangle$ is quite close to $\langle u'u' \rangle$ for each individual day, with the
exception of the data from February 26. In our simulations, horizontal vari-
ances are much smaller than vertical variances in the middle of the mixed
layer. The reverse is true in the surface layer, where shear-generated turbu-
lence dominates over convective turbulence.

3.1.2 Spectra

To investigate further the anisotropic behavior in the simulations, we have
calculated various one-dimensional velocity spectra. Let us define S_{11} as
the power spectrum of u along the x direction. Similarly, we can define
S_{22} as the power spectrum of v along the y direction. If the turbulence
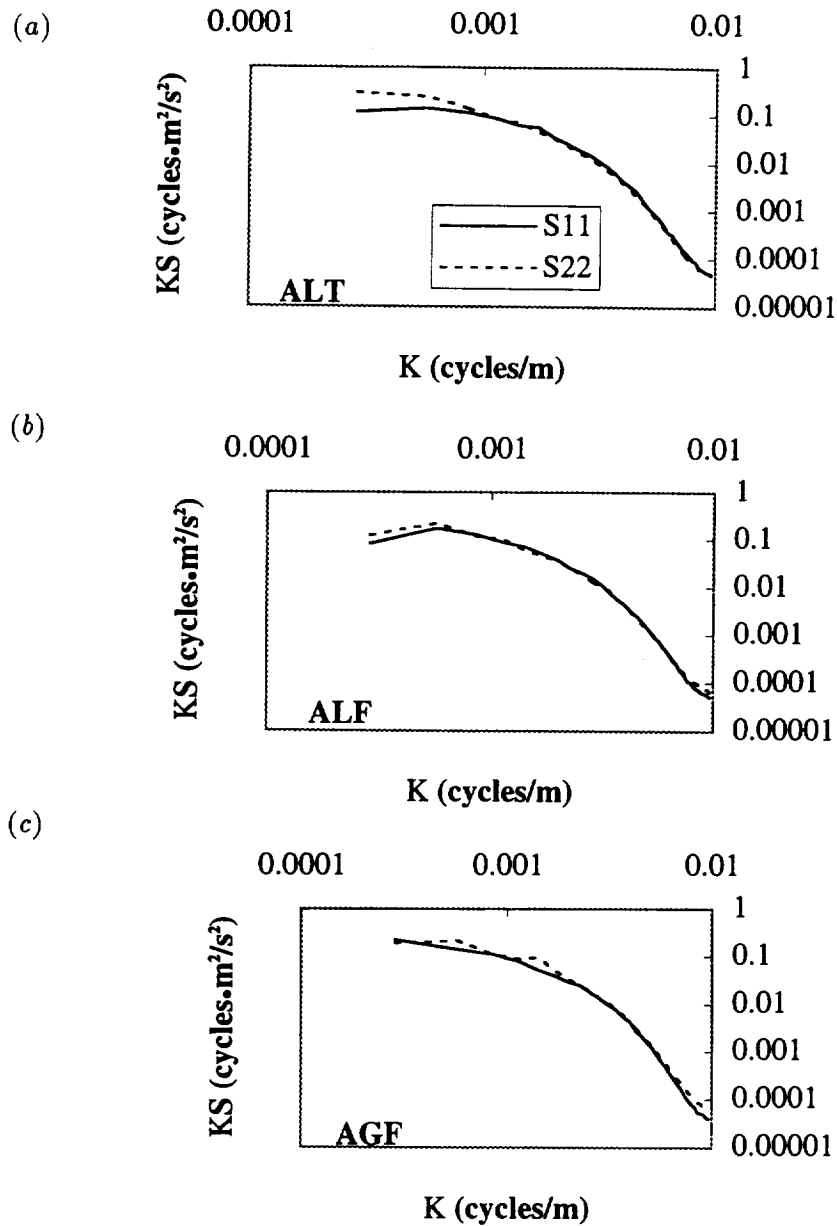
Figure 4: Longitudinal spectra at $z/Z_i = 0.12$ for (a) case ALT (local drag coefficient, surface temperature specified), (b) case ALF (local drag coefficient, surface flux uniformly specified), and (c) case AGF (global drag coefficient, surface flux uniformly specified).

14

in the mixed layer were horizontally isotropic, these two spectra would be identical. Figure 4 shows these spectra for the three cases discussed. Spectra were calculated for each longitudinal grid line at the specified height, then averaged in the other horizontal direction. That is, S_{11} was averaged in the y direction and S_{22} was averaged in the x direction. The spectra were also averaged in time in the same manner as the variances. We can determine the scales of the anisotropy by observing the wavenumbers for which S_{11} and S_{22} are different. For case ALT, the anisotropy near the surface occurs at the smallest wavenumbers, at length scales roughly the size of the domain. In fact, the spectral peak for S_{22} occurs at the domain size wavenumber. For case ALF, in which the surface flux was uniform, but the the drag coefficient nonhomogeneous, the anisotropy also occurs at the highest wavenumbers. It is worth noting, however, that a spectral peak above the domain size wavenumber does exist. Although Figure 2(c) shows some mild anisotropy near the surface for case AGF, Figure 4 (c) reveals that this is distributed throughout the wavenumber range.

Figure 5 shows the same spectral results near the top of the mixed layer. The curves for cases ALT and ALF are qualitatively similar at this height, but the spectra for case AGF show that the u variance is *larger* than the v variance at this height and at low wavenumbers. As previously stated, this is most likely due to shear production at the inversion. Thus, the evidence from the variances and the spectra point to a large scale anomaly in the cross-stream velocity deviation from the mean, both near the surface and near the inversion for local evaluation of the drag coefficient.
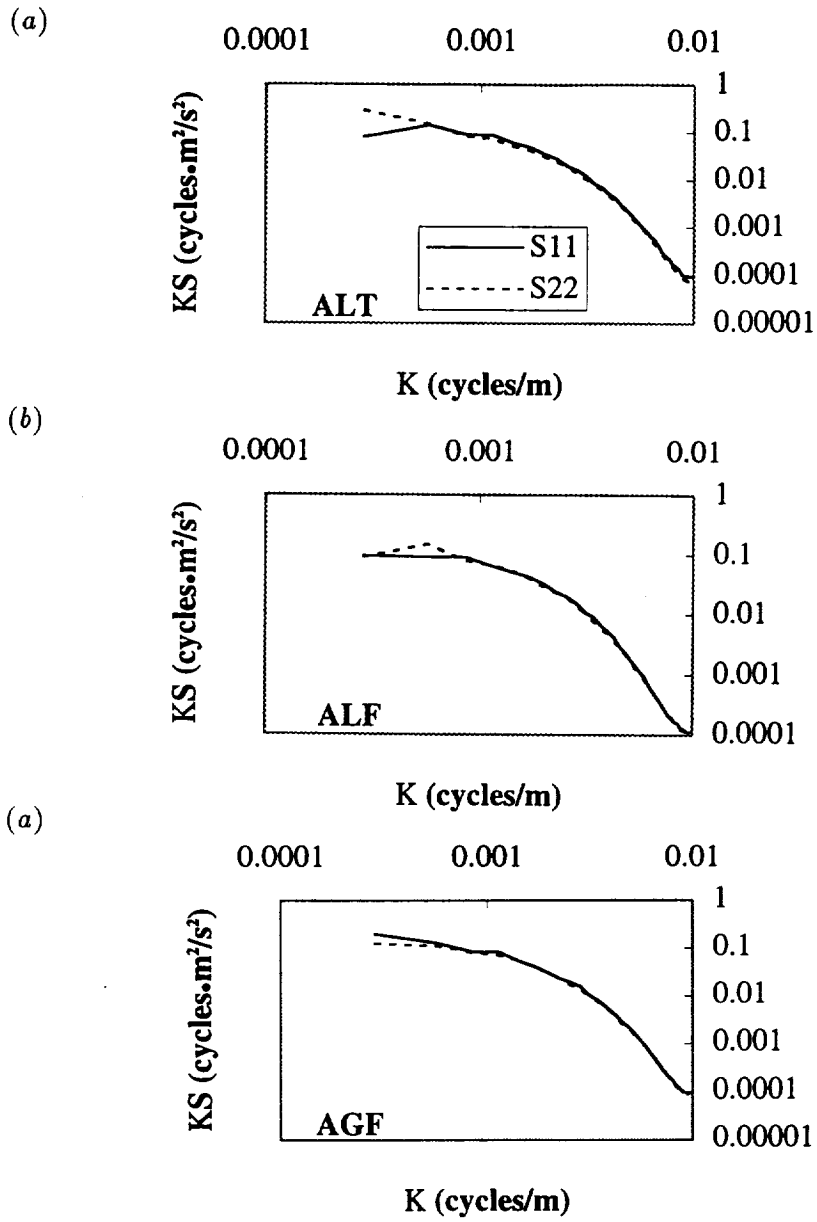
Figure 5: Same as figure 4 but for $z/Z_i = 0.86$.

16
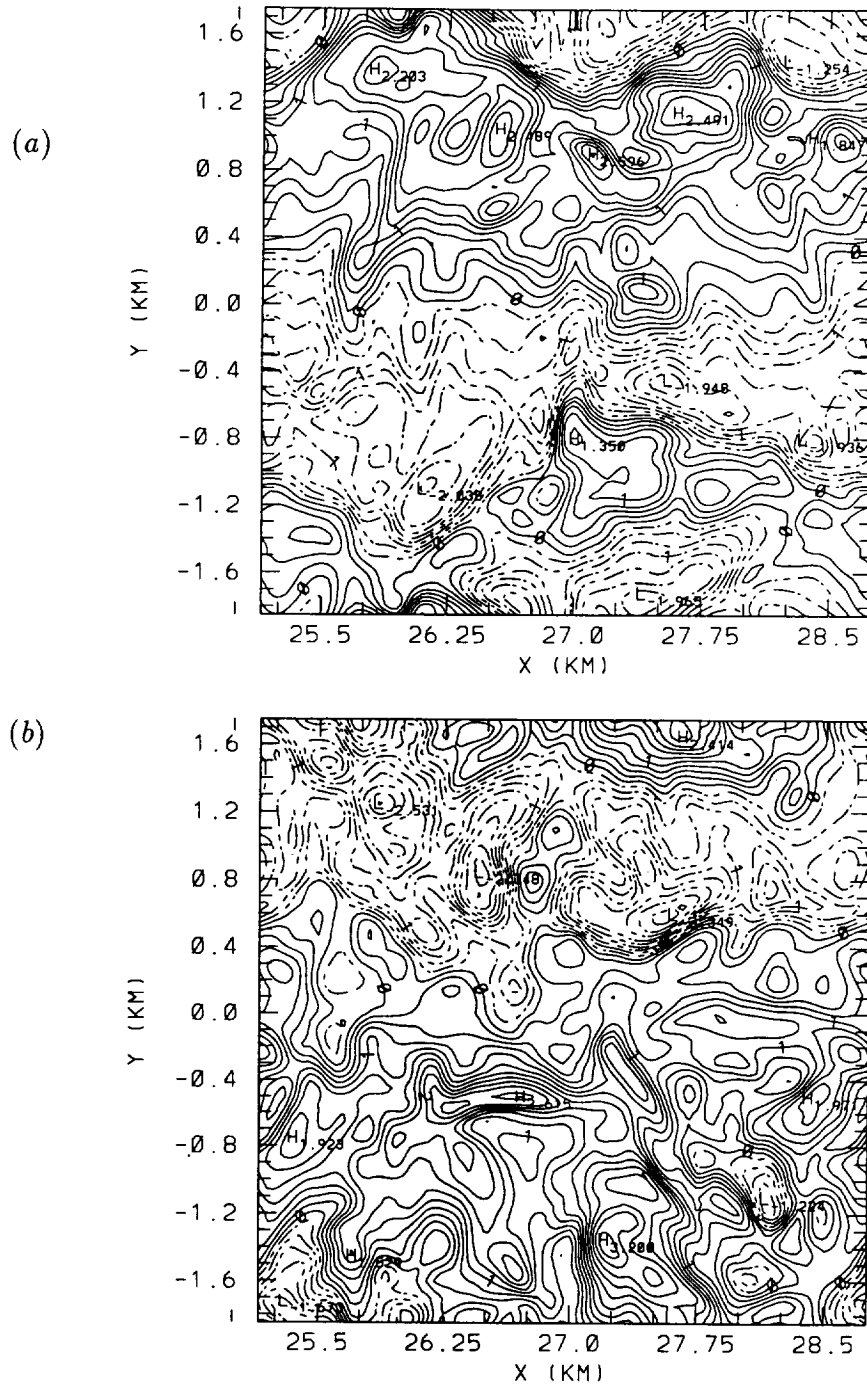
Figure 6: Contour plots of cross-stream velocity for case ALT after 150 minutes of simulation time. (a) $z/Z_i = 0.12$ (from -2.0 ms^{-1} to 2.5 ms^{-1} by 0.25) (b) $z/Z_i = 0.86$ (from -2.5 ms^{-1} to 3.0 ms^{-1} by 0.25). Negative contours are dashed.

Figure 7: Contour plots of vertical velocity after 150 minutes of simulation time for case ALT. (a) $z/Z_i = 0.47$ (from -2.0 ms^{-1} to 4.4 ms^{-1} by 0.4) (b) $z/Z_i = 0.04$ (from -1.8 ms^{-1} to 1.4 ms^{-1} by 0.2). Again, negative contours are dashed.

18
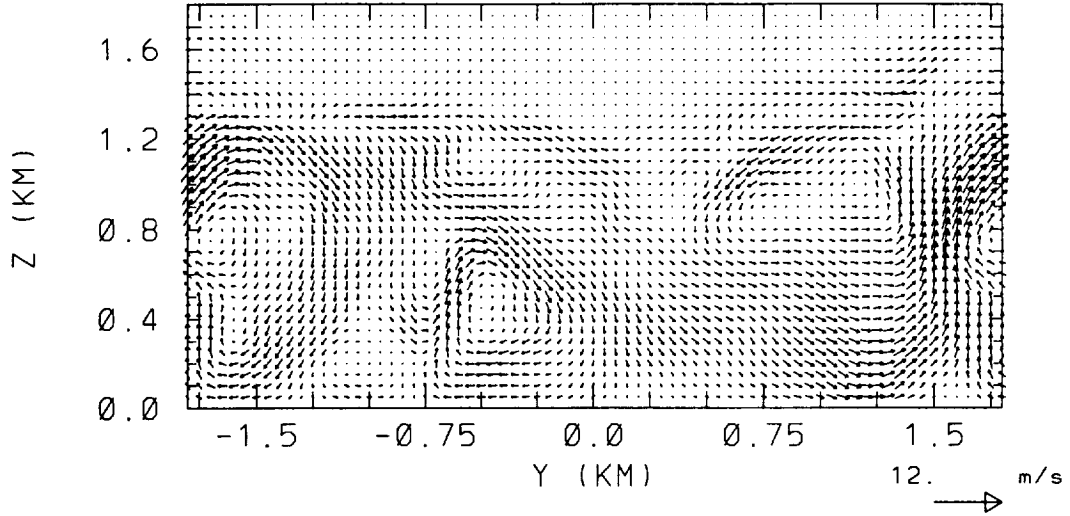
Figure 8: Velocity vectors at $x = 27.75$km for case ALT after 150 minutes of simulation time.

3.1.3 Instantaneous Velocity Contours

Contour plots of cross-stream velocity near the surface and at the inversion for case ALT in Figure 6 complete the picture of this anomaly. The cross-stream velocity contours show streaks aligned roughly in the streamwise direction, whose wavelength is the domain size. That is, in Figure 6(a), the cross-stream velocity is predominantly positive between $y = 0.4$ km and $y = 1.6$ km while it is predominantly negative elsewhere. In Figure 6(b), at the top of the mixed layer, the behavior is opposite in that the cross-stream velocity is predominantly negative between $y = 0.4$ km and $y = 1.6$ km and positive elsewhere. The vertical velocity also shows some streaky behavior. In Figure 7(a), we observe an updraft structure extending across the entire

domain in the x direction at $y \simeq 1.6$ km (the domain is horizontally periodic). Thus we seem to have streamwise roll vortices in which the dominant thermal structure is aligned with the mean wind. Near the ground, there is a strong positive cross-stream flow to the south of this structure and a strong negative cross-stream flow to the north. At the top of the mixed layer, this is reversed as the flow recirculates. This is also illustrated in Figure 8, a vector plot for a plane perpendicular to the mean flow direction. Here, again, we observe the dominant thermal structure at $y \simeq 1.6$ km with strong northerly and southerly flows feeding the plume from the bottom and exiting at the top of the mixed layer. This would account for the large anisotropies at these vertical levels. Although there is certainly some random behavior in these plots, they are only snapshots. The one hour averages of variance and spectra show the persistence of this behavior.

As a comparison, horizontal cross-sections of vertical velocity for case AGF, in which the drag coefficient was globally calculated, are shown in Figure 9. Here, we observe no clear streamwise structure. In addition, at $z/Z_i = 0.04$, we observe a spoke pattern in which the thermal structures consist of arms emanating from central nodes. There are well-defined nodes at (x,y) points (28.75,0.2), (26.25, -1.0), (27.0,1.2),and (27.75, -0.10). It is interesting to note that this spoke pattern of Rayleigh-Bénard type convection also observed by Schmidt and Schumann does not occur at $z/Z_i = 0.47$. Perhaps there is only a small part of the boundary layer in which this type of convection should be expected. This topic deserves further study and is beyond the scope of the present paper.
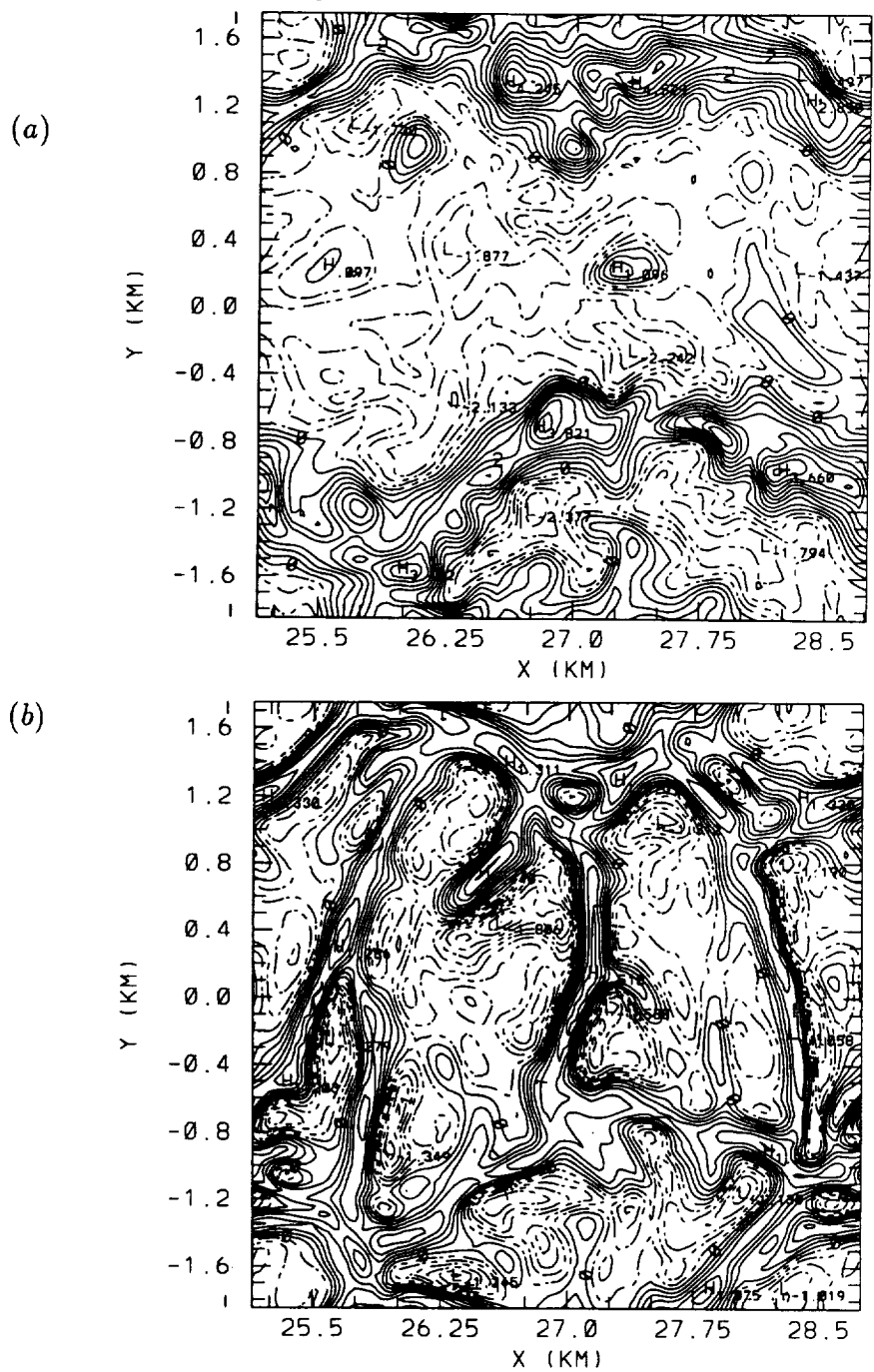
Figure 9: Contour plots of vertical velocity after 150 minutes of simulation time for case AGF. (a) $z/Z_i = 0.47$ (from -2.0 ms^{-1} to 4.0 ms^{-1} by 0.4) (b) $z/Z_i = 0.04$ (from -1.6 ms^{-1} to 1.4 ms^{-1} by 0.2).

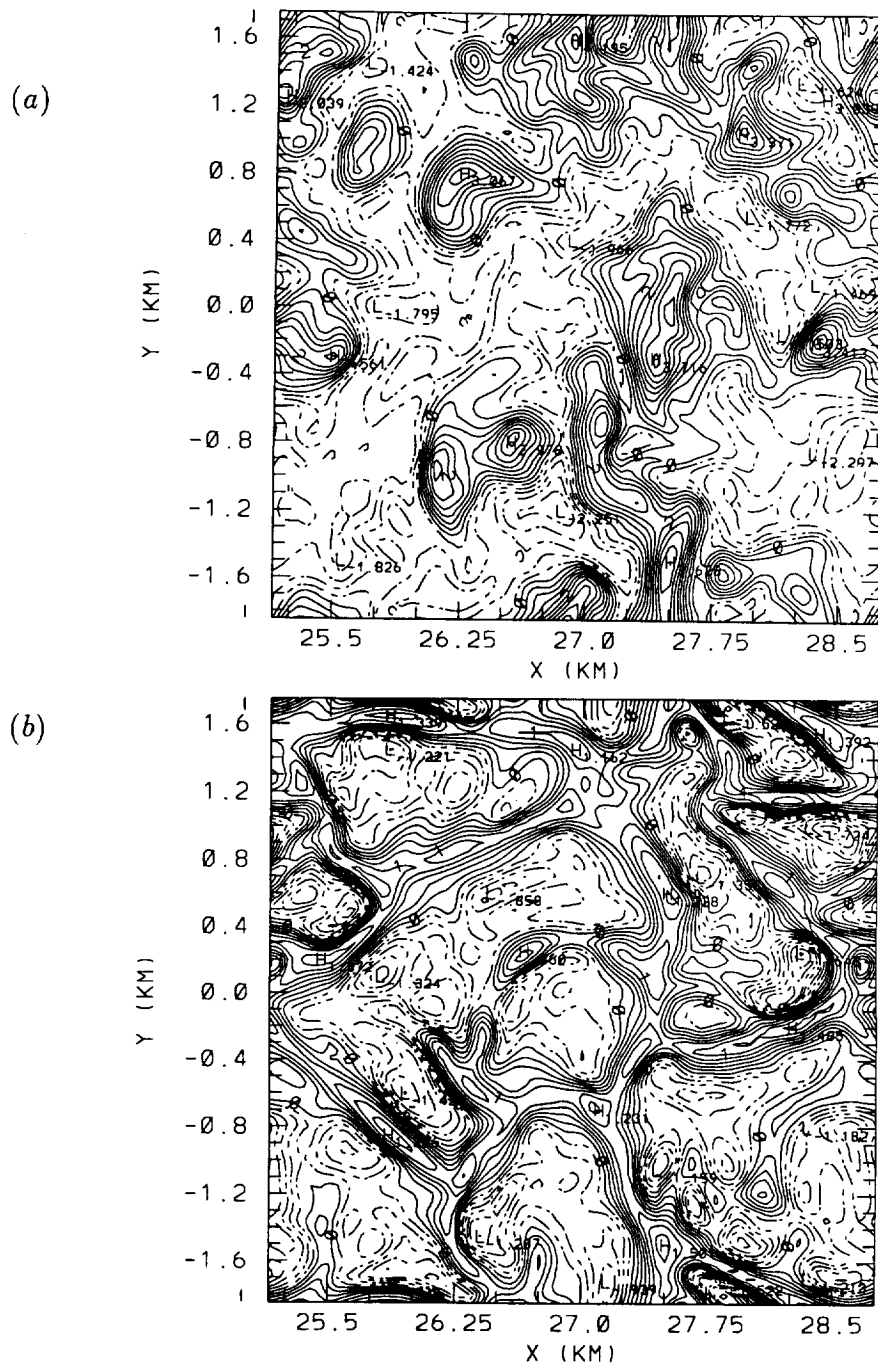Streamwise convective roll structures in the boundary layer have been documented (Rabin *et al.* 1982, Moeng and Sullivan 1994, Atlas *et al.* 1986). These usually occur, however, when shear and buoyancy are both important aspects of the flow. The present simulations have been highly convective. Asai's (1970) stability analysis showed that statically unstable fluid with an inflection point in the velocity profile ought to develop vortical flow structures *perpendicular* to the flow direction, rather than in the streamwise direction. It must be noted, however, that his analysis was linear and the current simulations as well as the flows in the above mentioned references were highly non-linear. A close look at Figure 3 and Table 2 reveals possible roll behavior for the February 26 case from Lenschow *et al.* Here, $Z_i/L = -13.2$, the smallest absolute value of all the cases, indicating that it was the least convective. Near the ground and near the inversion, $\langle v'v' \rangle$ is consistently larger than $\langle u'u' \rangle$, an observation indicative of streamwise rolls. For the present simulations, $Z_i/L = -301$, indicating highly convective conditions. Streamwise rolls would not be expected in this case. These appear to be an artifact of the lower boundary conditions in this particular simulation.

Figure 10 shows the drag coefficient for case ALT after 150 minutes of simulation time. The background shows the sign of the vertical velocity at 25 meters. By comparing with Figure 7(b), we observe the same vertical velocity structure in the background image. In addition, we see that the drag coefficient is highest primarily at the centers of the updraft regions and is lowest just outside of these regions. This is expected because the local velocity magnitude will be low in the centers of the updraft regions (this
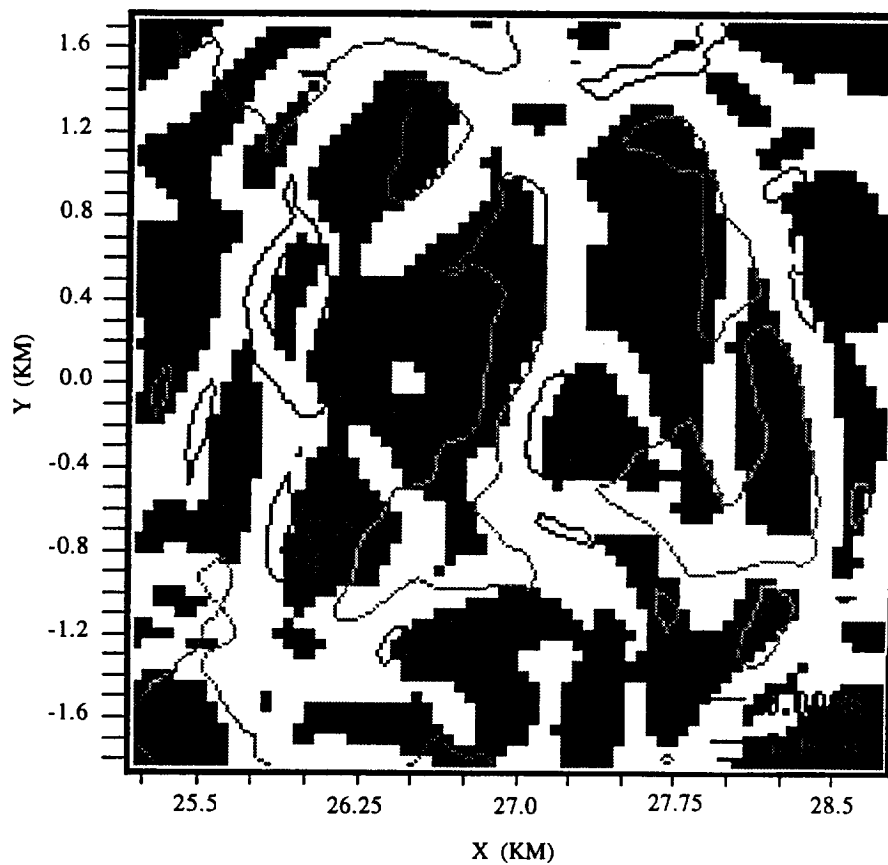
Figure 10: Contours of simulated surface drag coefficient after 150 minutes of simulation time for case ALT as a function of horizontal position. Black background indicates negative vertical velocity at $z = 25$ meters, while white background indicates positive vertical velocity.

23

leads to a smaller value of u_* and, hence, a smaller absolute value of the Obukhov length by Equation 18). Thus, there is a larger drag coefficient in these regions in the local case. By the same principal, the drag coefficient is expected to be relatively low at the entrance to the thermal plumes where there are strong horizontal velocities.

It is common in problems of fluid mechanics to have streamwise streaks in regions of high shear because the ambient strain rate tilts cross-stream vorticity into the streamwise direction (see, for example Lin and Corcos' 1984 discussion of streamwise vortices in shear layers). Under convective conditions, however, we hypothesize that the drag at the surface is large enough to destroy these structures. When the drag coefficient is calculated locally, the drag becomes low enough just outside the updraft regions to allow such structures to exist. There they may combine with the thermal plume structures.

Figures 4 and 5 show that often the most dominant scale was the domain size. This is true even for S_{11} in case AGF close to the ground. Because the anomalies typically scaled with the domain size, we believed that an increase in the horizontal extent of the domain may subdue the problem of the anisotropy with a local drag coefficient.

3.2   102 × 102 × 38 Domain

In these simulations, which are labeled as "B" in table 1, we have used the same grid resolution, but have increased the number of grid points horizontally such that the domain was 5100 m × 5100 m × 1900 m. This gave a horizontal extent of four times the boundary layer height during the aver-
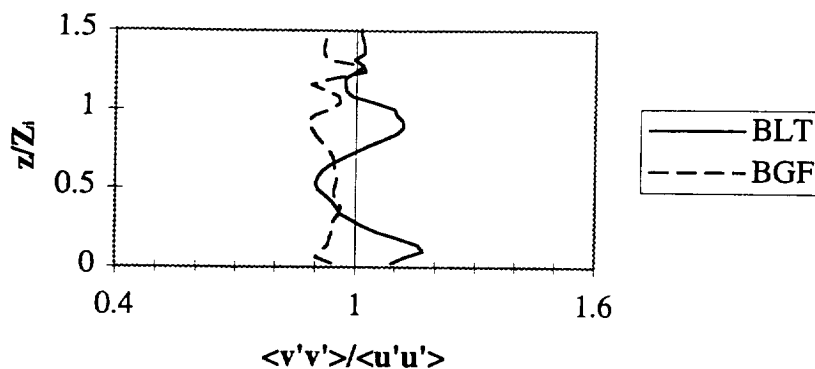
Figure 11: Horizontal anisotropy for cases BLT and BGF

aging period. Owing to the expense of running these simulations, we chose
two boundary conditions to test for this domain. Case BLT employed a local
drag coefficient and used a specified surface temperature. Case ALT showed
the most severe anisotropies, so we felt it was important to look at the effect
of domain size with the same boundary condition. We have not run a case
in which the drag coefficient was local and the surface flux was specified be-
cause the results of case ALF were qualitatively similar to ALT, though the
anisotropy was less severe. The second run for this domain was case BGF, in
which the drag coefficient was calculated globally and the flux was specified.
As in the smaller domain runs, the mean surface flux as a function of time
was extracted from case BLT and used for case BGF.

Figure 11 shows the horizontal anisotropy for cases BLT and BGF. Note
that case BLT is not as anisotropic as case ALT, but that the trend is the
same. There remain large anisotropies close to the ground and just below
the inversion. Spectra for these cases are shown in Figure 12. There is a well

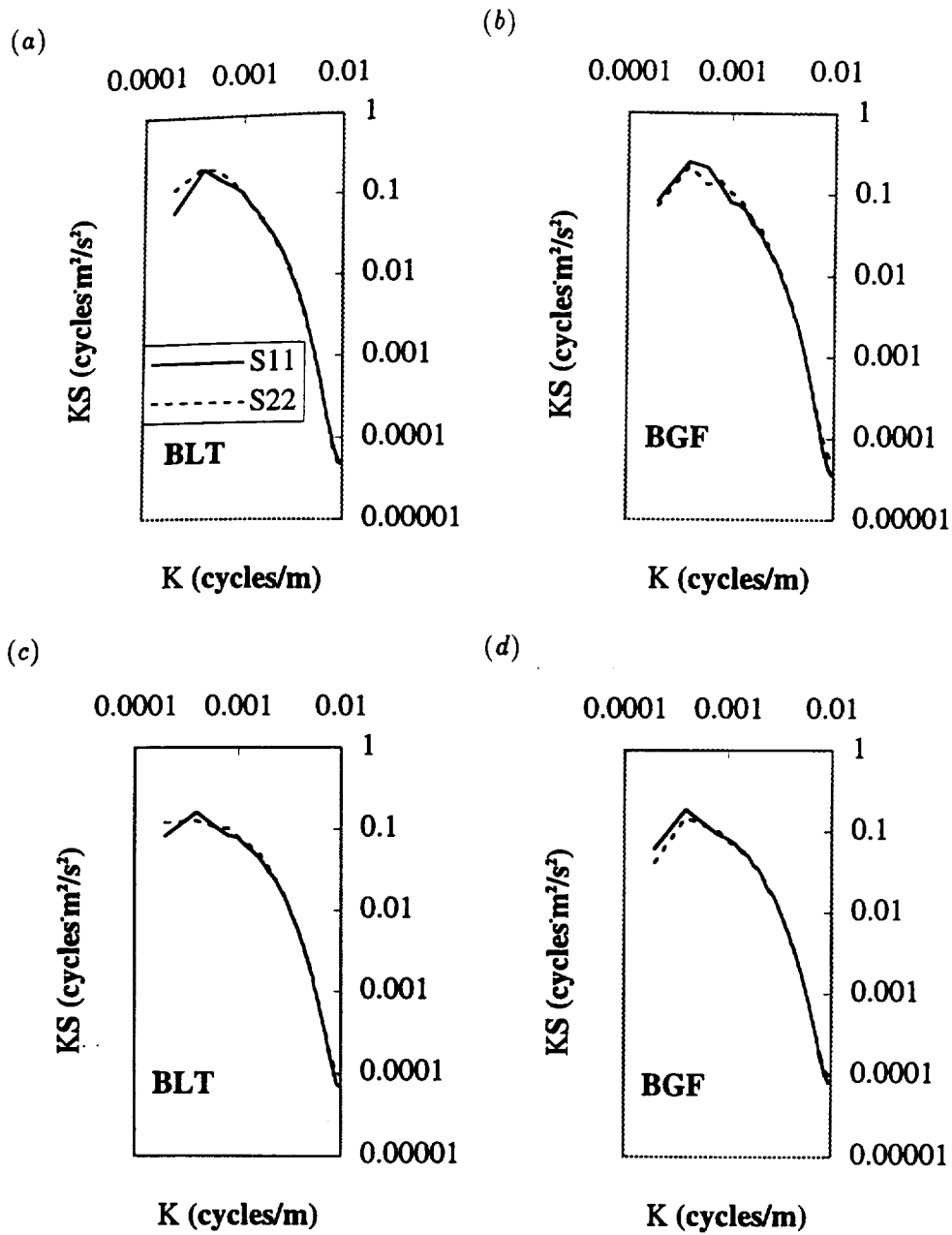Figure 12: Longitudinal spectra for (a) case BLT at z/Z_i = 0.12, (b) case BGF at z/Z_i = 0.12, (c) case BLT at z/Z_i = 0.86, and (d) case BGF at z/Z_i = 0.86.

defined spectral peak for S_{11} in all cases. In case BLT, however, the spectral peak is not as well defined for S_{22} at $z/Z_i = 0.12$ and not at all defined for $z/Z_i = 0.86$. For case BGF, however, in which the drag coefficient was global, S_{22} has a defined peak at both levels. Thus, increasing the size of the domain improved the local drag coefficient results, but did not eliminate the problem of the anomalous streamwise rolls.

Another parameter that we believed may have had an important effect was the vertical resolution of the grid mesh.

3.3   80 × 80 × 72 Domain

For these cases, labeled "C," the vertical grid resolution was increased to 25 meters. The first grid level was 12.5 meters above the surface. The horizontal resolution remained at 50 meters. Thus, the horizontal domain size was 4000 meters, about 3.1 times the inversion height during the averaging period. We believed that stress would be calculated more accurately with points closer to the surface. Again, only cases CLT (local drag coefficient calculation, surface temperature specified) and CGF (global drag coefficient, surface heat flux specified) were run, owing to the computational expense.

The anisotropy for these two cases is shown in Figure 13. Here we observe that this increased vertical resolution had a profound effect on the anomaly. Case CLT shows stronger anisotropy close to the ground, but CGF gives $\langle v'v' \rangle < \langle u'u' \rangle$ at two-thirds of the inversion height. At $z/Z_i = 1$, CLT again shows a positive anisotropy, but the magnitude is much smaller than for case BLT.

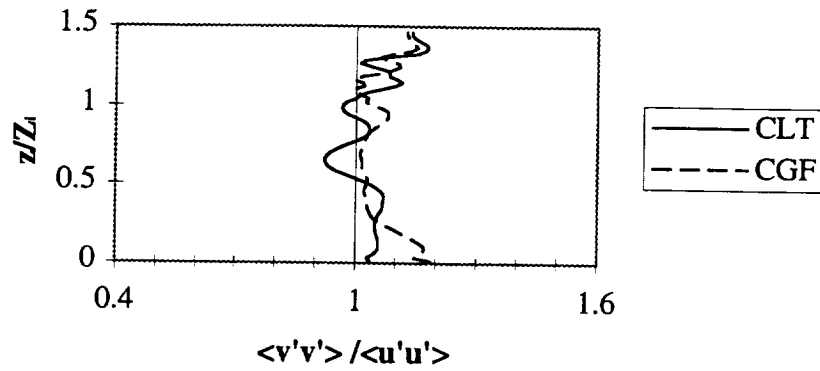Figure 14, a contour plot of vertical velocity at $z/Z_i = 0.04$ for case CLT,

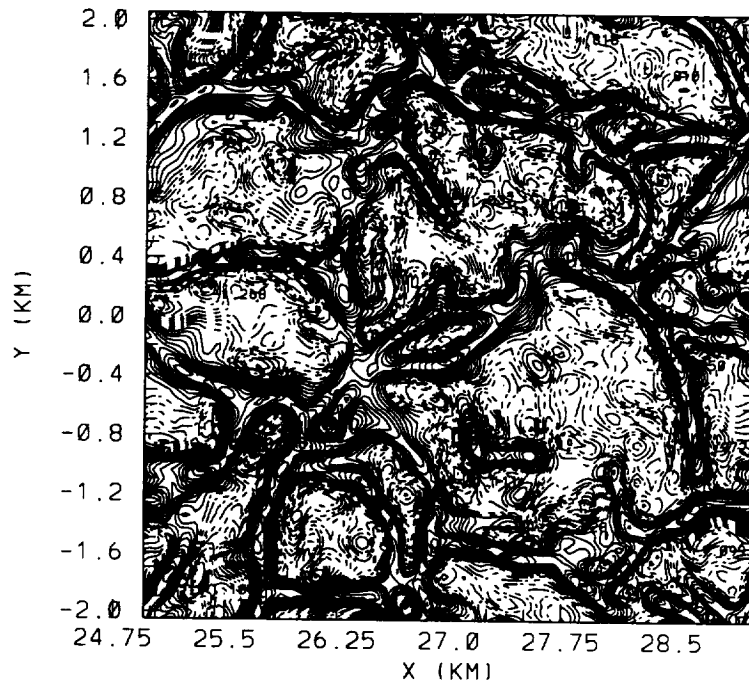Figure 13: Anisotropy for cases CLT and CGF with increased vertical resolution.

Figure 14: Contour plot of vertical velocity after 150 minutes of simulation time for case CLT at $z/Z_i = 0.04$ (from -1.4 ms^{-1} to 1.4 ms^{-1} by 0.1).
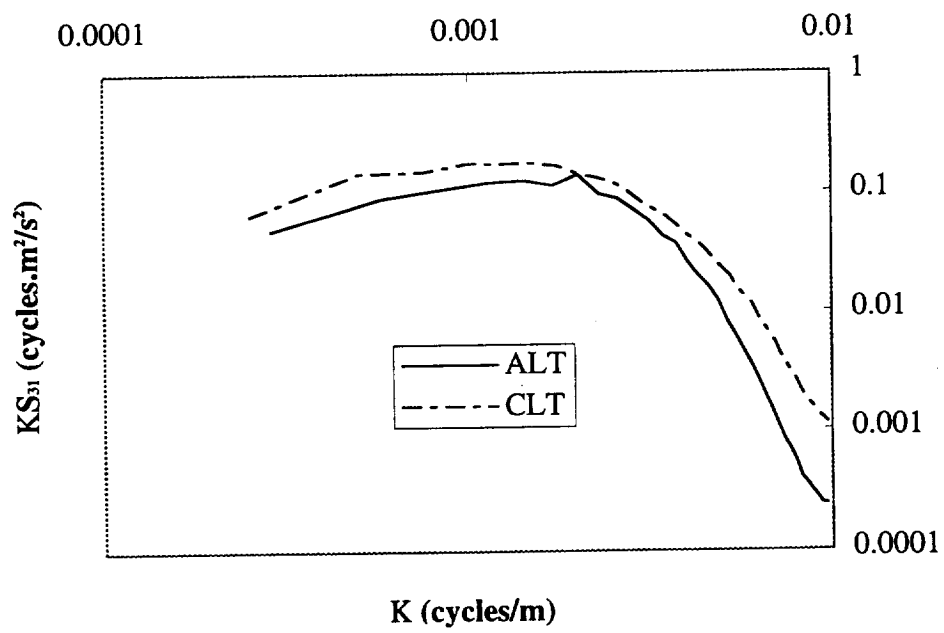
Figure 15: Longitudinal vertical velocity spectra, S_{31} at $z/Z_i = 0.12$ for cases ALT and CLT.

presents a possible reason for this improved behavior. Upon comparison with Figure 7(b) from case ALT, we note that there appears to be finer scale structures in case CLT, even though the horizontal resolution has remained constant. Indeed, the S_{31} spectra in Figure 15 show this to be the case (S_{31} being the spectrum of vertical velocity in the streamwise direction). The high wavenumber end of the spectrum contains considerably more energy at this height for case CLT. Thus, when the vertical grid spacing was large in case ALT, the flow close to the ground seemed to depend too strongly upon the similarity boundary condition and important scales of eddies were not resolved. It appears that the small scale eddies close to the ground in case CLT prevented the longitudinal rolls from dominating the flow structure.

4 Conclusions

In conclusion, we have observed that using a locally calculated drag coefficient at the surface of a large-eddy simulation model led to unrealistically large horizontal anisotropies in convective boundary layer turbulence, especially when coarse vertical resolution was used in combination with a small horizontal domain extent. This anisotropy was due to large scale streamwise rolls which are typically found in boundary layers in which shear and buoyancy are equally important. In the reported cases, however, buoyancy was clearly dominant and the rolls were not expected. The rolls occurred because the drag coefficient was smallest at the entrance to large scale thermal structures. Thus, the streamwise streak structure which is common in shear flows was not destroyed by the stress at the ground in those regions. It is

30

hypothesized that in these low drag coefficient regions close to the thermals, streamwise vortices are allowed to exist and combine with the plumes.

The dominance of these structures was most clear when the surface heat flux was nonhomogeneous and depended upon the local temperature difference between surface and atmosphere. It was noticeable, however, even when the surface heat flux was uniform but the drag coefficient was locally derived. Increasing the horizontal domain size such that it was four inversion heights wide improved the results. Increasing the vertical resolution such that the first grid point was 12.5 meters above the surface as opposed to 25 meters rendered the anisotropy almost imperceptable. This is likely owing to the finer scale resolved eddies which appeared close to the ground in this case. Thus, when the vertical grid spacing was too large, important scales of turbulence were unresolved, facilitating the formation of the more regular, longitudinal rolls.

In closing, we note that, although temperature specification led to a larger anomaly than did flux specification for the local drag coefficient cases, it made very little difference if the drag coefficient was global. A test case which could have been called AGT (global drag coefficient, surface temperature specified) was run and the results were not significantly different from case AGF. Thus, the temperature specification only affects the flow insofar as the local temperature differences lead to inhomogeneous surface heat fluxes and inhomogeneous drag coefficients.

A Calculation of surface heat flux from surface temperature

The details of calculating surface heat fluxes from surface temperatures are described below. The method was derived from equations in Arya (1988). First, the heat flux was defined globally or locally as

$$(\overline{w'\theta'})_s = -u_*\theta_* \tag{20}$$

where u_* is defined by (17) or (19) and

$$\theta_* = \frac{k\{\theta_a - \theta_s\}}{\alpha_0\{\ln(z_a/z_s) - \Psi_H(z_a/L) + \Psi_H(z_s/L)\}}, \tag{21}$$

where we have used a value of 0.4 for k. θ_a is the potential temperature at the first grid level above the surface in the model. As in Section 2, local values of velocity and temperature were used for local drag coefficients and heat fluxes, but horizontally averaged values are used here in the global case. That is, for global calculation of θ_*, $\langle\theta_a\rangle$ was used in place of θ_a. In either case, θ_s is the given uniform potential temperature at z_s, some level between 0 and z_a. For L, the Obukhov length, (16) or (18) was used. We have used a value of 0.89 for α_0, the surface turbulent Prandtl number. For the stability functions, we use the following relations:

$$\Psi_M(z/L) = \Psi_H(z/L) = -5z/L \qquad z/L \geq 0 \tag{22}$$

$$\Psi_M(z/L) = 2\ln(\frac{1+x}{2}) + \ln(\frac{1+x^2}{2})$$
$$- 2\arctan(x) + \pi/2 \qquad z/L < 0 \tag{23}$$

32

$$\Psi_H(z/L) = 2\ln(\frac{1+x^2}{2}) \qquad z/L < 0 \qquad (24)$$

where

$$x = (1 - 15z/L)^{1/4}. \qquad (25)$$

In the case of a local drag coefficient, a polynomial approximation to the above stability functions was used for computational efficiency.

References

[1] Arya, S. P.: 1988, 'Introduction to Micrometeorology', Academic Press, San Diego.

[2] Asai, T.: 1970, 'Stability of a Plane Parallel Flow with Variable Vertical Shear and Unstable Stratification', *J. Meteor. Soc. Japan*, **48**, 129-139.

[3] Atlas, D., Walter, B., Chou, S.-H., Sheu, P.J.: 1986, 'The Structure of the Unstable Marine Boundary Layer Viewed by Lidar and Aircraft Observations', *J. Atmos. Sci.*, **43**, 1301-1318.

[4] Clarke, R. H., Dyer, A. J., Brook, R. R., Reid, D. G., and Troup, A. J.: 1971, 'The Wangara Experiment: Boundary Layer Data', CSIRO Div. of Meteorol. Phys. Tech. Paper No. 19.

[5] Deardorff, J. W.: 1973,'Three-Dimensional Numerical Modeling of the Planetary Boundary Layer', *Workshop on Micrometeorology*, D. A. Haugen, ed., American Meteorology Society, 271-311.

[6] Deardorff, J. W.: 1974,'Three-Dimensional Numerical Study of Turbulence in an Entraining Mixed Layer', *Bound. Layer Meteor.*, **7**, 199-226.

[7] Hechtel, L. M., Moeng, C.-H. and Stull, R. B.: 1990, 'The Effects of Nonhomogeneous Surface Fluxes on the Convective Boundary Layer: A Case Study Using Large-Eddy Simulation', *J. Atmos. Sci.*, **47**, 1721-1741.

[8] Hinton, D. A.: 1995, 'Aircraft Vortex Spacing System (AVOSS) Conceptual Design', NASA Tech. Memo. 110184.

[9] Lenschow, D. H., Wyngaard, J. C. and Pennell, W. T.: 1980, 'Mean-Field and Second-Moment Budgets in a Baroclinic, Convective Boundary Layer', *J. Atmos. Sci.*, **37**, 1313-1326.

[10] Lin, S.J. and Corcos, G.M.: 1984, 'The Mixing Layer: Deterministic Models of a Turbulent Flow. Part 3. The Effect of Plane Strain on the Dynamics of Streamwise Vortices', *J. Fluid Mech.*, **141**, 139.

[11] Mason, P. J.: 1989,'Large-Eddy Simulation of the Convective Atmospheric Boundary Layer', *J. Atmos. Sci.*,**46**, 1492-1516.

[12] Mason, P. J., and Thomson, D. J.: 1992, 'Stochastic Backscatter in Large-Eddy Simulation of Boundary Layers', *J. Fluid Mech.*, **242**, 51-78.

[13] Moeng, C.-H.: 1984,'A Large-Eddy Simulation Model for the Study of Planetary Boundary Layer Turbulence', *J. Atmos. Sci.*, **41**, 2052-2062.

[14] Moeng, C.-H., and Sullivan, P. P.: 1994, 'A Comparison of Shear- and Buoyancy-Driven Planetary Boundary Layer Flows', *J. Atmos. Sci.*,**51**, 999-1022.

[15] Paulson, C. A.: 1970, 'The Mathematical Representation of Wind Speed and Temperature Profiles in the Unstable Atmospheric Surface Layer', *J. Applied Meteor.*, **9**,857-861.

[16] Proctor, F. H.: 1988, 'Numerical Simulations of an Isolated Microburst. Part I: Dynamics and Structure', *J. Atmos. Sci.*, **45**, 3137-3159.

[17] Proctor, F. H., and Bowles, R. L.: 1992, 'Three-dimensional simulation of the Denver 11 July 1988 microburst-producing storm', *Meteorol. and Atmos. Phys.*, **49**, 107-124.

[18] Rabin, R. M., Doviak, R. J., and Sundara-Rajan, A.: 1982, 'Doppler Radar Observations of Momentum Flux in a Cloudless Convective Layer With Rolls', *J. Atmos. Sci.*, **39**, 851-863.

[19] Schmidt, H. and Schumann, U.: 1989, 'Coherent Structure of the Convective Boundary Layer Derived From Large-Eddy Simulations', *J. Fluid Mech.*, **200**, 511-562.

[20] Schowalter, D. G., DeCroix, D. S., Lin, Y.-L., Proctor, F. H., Arya, S. P., and Kaplan, M. L.: 1995. 'Turbulent Statistics in the Atmospheric Boundary Layer: A Comparison of Large Eddy Simulation With Observations.' *11th Symp. Bound. Layers Turb.*, American Meteorological Society, 552-555.

[21] Shen, S. and Leclerc, M. Y.: 1994, 'Large-Eddy Simulation of Small-Scale Surface Effects on the Convective Boundary-Layer Structure', *Atmosphere-Ocean*, **32**, 717-731.

[22] Shen, S. and Leclerc, M. Y.: 1995, 'How Large Must Surface Inhomogeneities Be Before They Influence the Convective Boundary Layer Structure? A Case Study', *Q.J.R. Meteorol. Soc.*, **121**, 1209-1228.

REPORT DOCUMENTATION PAGE

Public reporting burden for this collection of information is estimated to average 1 hour per response, including the time for reviewing instructions, searching existing data sources, gathering and maintaining the data needed, and completing and reviewing the collection of information. Send comments regarding this burden estimate or any other aspect of this collection of information, including suggestions for reducing this burden, to Washington Headquarters Services, Directorate for Information Operations and Reports, 1215 Jefferson Davis Highway, Suite 1204, Arlington, VA 22202-4302, and to the Office of Management and Budget, Paperwork Reduction Project (0704-0188), Washington, DC 20503.

1. AGENCY USE ONLY (Leave blank)	2. REPORT DATE	3. REPORT TYPE AND DATES COVERED
	April 1996	Contractor Report

4. TITLE AND SUBTITLE

The Sensitivity of Large-Eddy Simulation to Local and Nonlocal Drag Coefficients at the Lower Boundary

5. FUNDING NUMBERS

NCC1-188
538-04-11-11

6. AUTHOR(S)

D. G. Schowalter, D. S. DeCroix, Y. L. Lin, S. P. Arya, and M. L. Kaplan

7. PERFORMING ORGANIZATION NAME(S) AND ADDRESS(ES)

Department of Marine, Earth and Atmospheric Sciences
North Carolina State University
Box 8208
Raleigh, NC 27695-8208

8. PERFORMING ORGANIZATION REPORT NUMBER

9. SPONSORING / MONITORING AGENCY NAME(S) AND ADDRESS(ES)

National Aeronautics and Space Administration
Langley Research Center
Hampton, VA 23681-0001

10. SPONSORING / MONITORING AGENCY REPORT NUMBER

NASA CR-198310

11. SUPPLEMENTARY NOTES

Langley Technical Monitor: Fred H. Proctor

12a. DISTRIBUTION / AVAILABILITY STATEMENT

Unclassified-Unlimited

Subject Category 34

12b. DISTRIBUTION CODE

13. ABSTRACT (Maximum 200 words)

It was found that the homogeneity of the surface drag coefficient plays an important role in the large scale structure of turbulence in large-eddy simulation of the covective atmospheric boundary layer. Particularly when a ground surface temperature was specified, large horizontal anisotropies occurred when the drag coefficient depended upon local velocities and heat fluxes. This was due to the formation of streamwise roll structues in the boundary layer. In reality, these structures have been found to form when shear is approximately balanced by buoyancy. The present cases, however, were highly convective. The formation was caused by particularly low values of the drag coefficient at the entrance to thermal plume structures.

14. SUBJECT TERMS

Large-eddy simulation; Planetary boundary layer; Model boundary conditions; Turbulence; Aircraft wake vortices.

15. NUMBER OF PAGES

43

16. PRICE CODE

A03

17. SECURITY CLASSIFICATION OF REPORT	18. SECURITY CLASSIFICATION OF THIS PAGE	19. SECURITY CLASSIFICATION OF ABSTRACT	20. LIMITATION OF ABSTRACT
Unclassified	Unclassified	Unclassified	